ACS APPLIED MATERIALS & INTERFACES

www.acsami.org

Research Article

Ferroelectric Proximity Effect and Topological Hall Effect in $SrRuO_3$/$BiFeO_3$ Multilayers

Xiaokang Yao, Can Wang,* Er-Jia Guo, Xinyan Wang, Xiaomei Li, Lei Liao, Yong Zhou, Shan Lin, Qiao Jin, Chen Ge, Meng He, Xuedong Bai, Peng Gao, Guozhen Yang, and Kui-juan Jin*

Cite This: *ACS Appl. Mater. Interfaces* 2022, 14, 6194−6202

Read Online

ACCESS | Metrics & More | Article Recommendations | Supporting Information

ABSTRACT: Interfaces between complex oxides provide a unique opportunity to discover novel interfacial physics and functionalities. Here, we fabricate the multilayers of itinerant ferromagnet $SrRuO_3$ (SRO) and multiferroic $BiFeO_3$ (BFO) with atomically sharp interfaces. Atomically resolved transmission electron microscopy reveals that a large ionic displacement in BFO can penetrate into SRO layers near the BFO/SRO interfaces to a depth of 2−3 unit cells, indicating the ferroelectric proximity effect. A topological Hall effect is indicated by hump-like anomalies in the Hall measurements of the multilayer with a moderate thickness of the SRO layer. With magnetic measurements, it can be further confirmed that each SRO layer in the multilayers can be divided into interfacial and middle regions, which possess different magnetic ground states. Our work highlights the key role of functional heterointerfaces in exotic properties and provides an important guideline to design spintronic devices based on magnetic skyrmions.

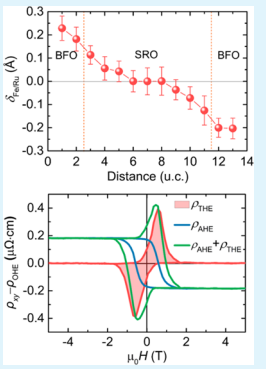

KEYWORDS: *complex oxides, interfacial physics, ferroelectric proximity effect, transport, magnetism*

1. INTRODUCTION

Interfaces between two distinct oxides have been a key point of interest in both fundamental research and device applications. Ultrathin regions within oxides near the interfaces often exhibit novel electrical and magnetic properties that are different from inherent properties of its bulk region, arising from the coupling of lattice, orbital, charge, and spin degrees of freedom across the heterointerfaces. Some intriguing phenomena, such as two-dimensional electron gas,[1] superconductivity,[2,3] and magneto-electric coupling,[4] have been observed at their heterointerfaces, playing a critical role in the current electronic devices.

Perovskite oxide $SrRuO_3$ (SRO), an itinerant ferromagnet with a Curie temperature (T_c) of 160 K and a low-temperature saturation magnetization of 1.6 μ_B/Ru,[5] often serves as an electrode material due to its high metallic conductivity and chemical stability. In bulk, SRO shows an orthorhombically distorted phase with the symmetry group *Pbnm* at room temperature.[6] The electrical transport and magnetic properties of SRO films are strongly dependent on the structural parameters, which can be controlled by strain induced by the residual lattice mismatch.[7,8] Previous works show that an insulating state is observed when the SRO thickness is less than 3−4 unit cells (u.c.).[9−11] They attribute the metastable phase in SRO with shrinking dimensionality to the structure disorder from the heterointerface. Recently, magnetic skyrmions, a nanoscale swirling spin texture, have been observed at low temperatures and under large applied magnetic fields, stimulating an increasing interest for their rich physics and potential applications in spintronics.[12] The topological Hall effect (THE) as a result of skyrmions is often inferred from the observation of hump-like anomalies in Hall measurements. Several studies have reported the THE in ultrathin SRO heterostructures,[13−20] which are driven by the strong interfacial Dzyaloshinskii−Moriya interaction (DMI) due to the broken inversion symmetry and spin−orbit coupling. It has been revealed that in a $BaTiO_3$ (BTO)/SRO heterointerface, ferroelectric-driven ionic displacements in BTO can penetrate into SRO near the interface, resulting in a displacement between Ru and O along the [001] axis.[16,20,21] This ferroelectric-driven lattice distortion breaks the inversion symmetry of the SRO structure near the interface, inducing a strong DMI, which is the driving force for the formation of skyrmions. Moreover, van Thiel et al.[22] reported that charge discontinuity in the SRO/$LaAlO_3$ interface can result in the broken inversion symmetry, thus inducing both magnetic and topological reconstruction in the SRO layer. Nonetheless, the hump-like Hall signal may also result from SRO inhomogeneity and can be explained by a two-channel anomalous Hall effect (AHE) model.[23−26] Ren et al.[25] reported that the

Received: November 9, 2021
Accepted: January 24, 2022
Published: January 24, 2022

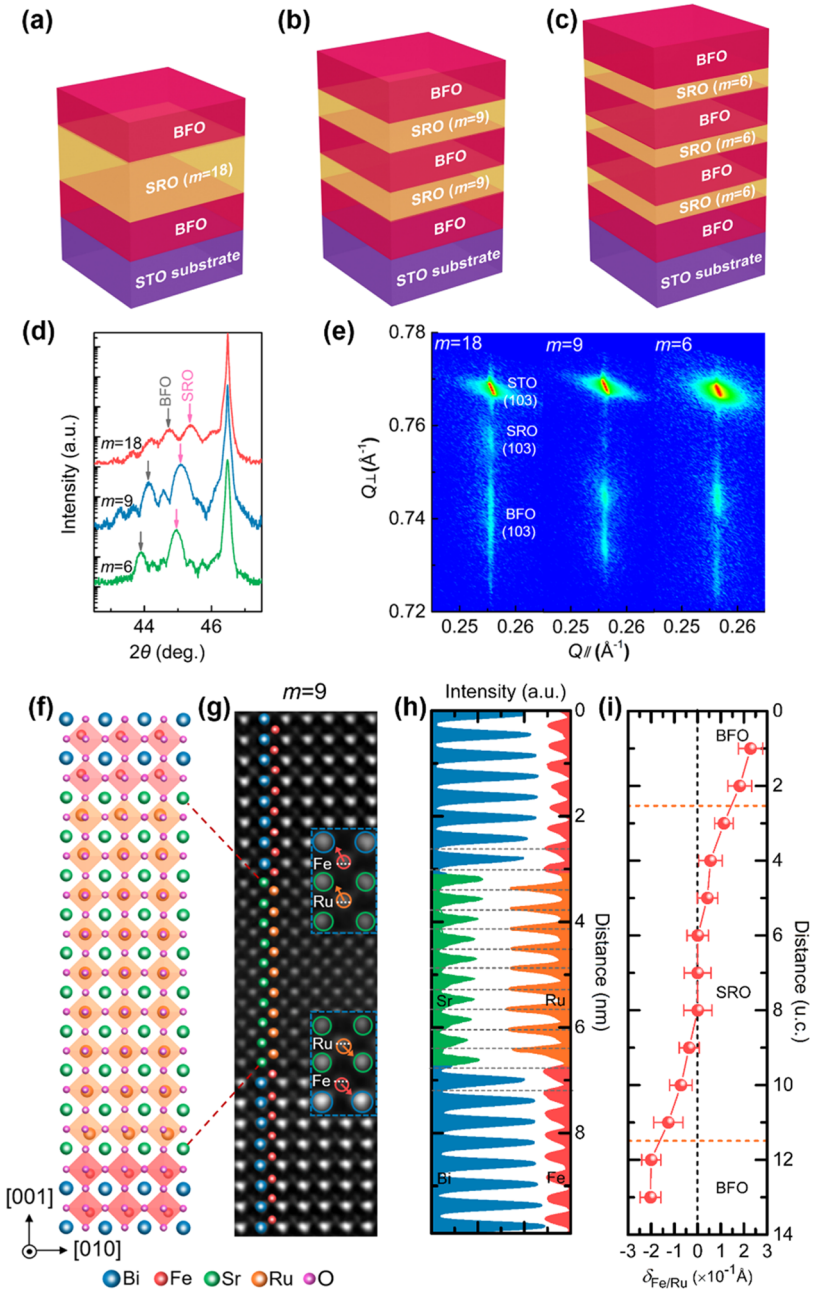

Figure 1. Structural characterization of SRO/BFO multilayers. Schematics of (a) m = 18, (b) m = 9, and (c) m = 6 samples grown on STO substrates, where m represents the number of unit cells. (d) XRD θ–2θ scans around the $(002)_{pc}$ peaks for the m = 18, 9, and 6 samples. (e) RSM results for the m = 18, 9, and 6 samples around the STO (103) diffraction condition. (f) Schematic diagram of the ionic displacements in the interfacial SRO regions. The blue, red, green, orange, and magenta spheres denote the Bi, Fe, Sr, Ru, and O atoms, respectively. (g) Atomic-scale high-resolution high-angle annular dark-field-STEM (HAADF-STEM) image for the m = 9 sample taken along the [100] axis of the substrates. Insets are the magnified images at the interfaces and the displacement vector of B-site cations with respect to the mass center of four nearest A-site cations. (h) The HAADF-STEM intensity profiles obtained from the corresponding A-site (Sr, Bi) and B-site (Ru, Fe) atomic columns. The white and gray dotted lines in (g, h) represent the center of A-site atoms. (i) Ionic displacement ($\delta_{Fe/Ru}$) along the [001] axis is extracted from the HAADF-STEM image of the m = 9 sample. The error bars represent the standard deviations of the averaged measurements for each vertical atomic layer.

observed nonmonotonic anomalous Hall resistivity behavior in the BFO/SRO bilayer system can be attributed to SRO inhomogeneity instead of THE. Ko et al.[26] found that the stoichiometry and lattice deformation of the SRO layer can be manipulated by controlling the growth pressure of the $LaAlO_3$ capping layer, thus resulting in two-channel AHE signals.

In this work, we present a design of multilayer structures of SRO and $BiFeO_3$ (BFO), where each SRO layer is sandwiched between two BFO layers, to investigate the interface effects on SRO transport and magnetic properties. BFO as a promising multiferroic material possesses strong ferroelectric polarization and G-type antiferromagnetic order at room temperature.[27−29] A series of SRO/BFO multilayers were fabricated by fixing the total thickness of SRO in the multilayers but varying the thickness of the single SRO layer. The ferroelectric proximity effect was revealed by atomically resolved scanning trans-

https://doi.org/10.1021/acsami.1c21703
ACS Appl. Mater. Interfaces 2022, 14, 6194−6202

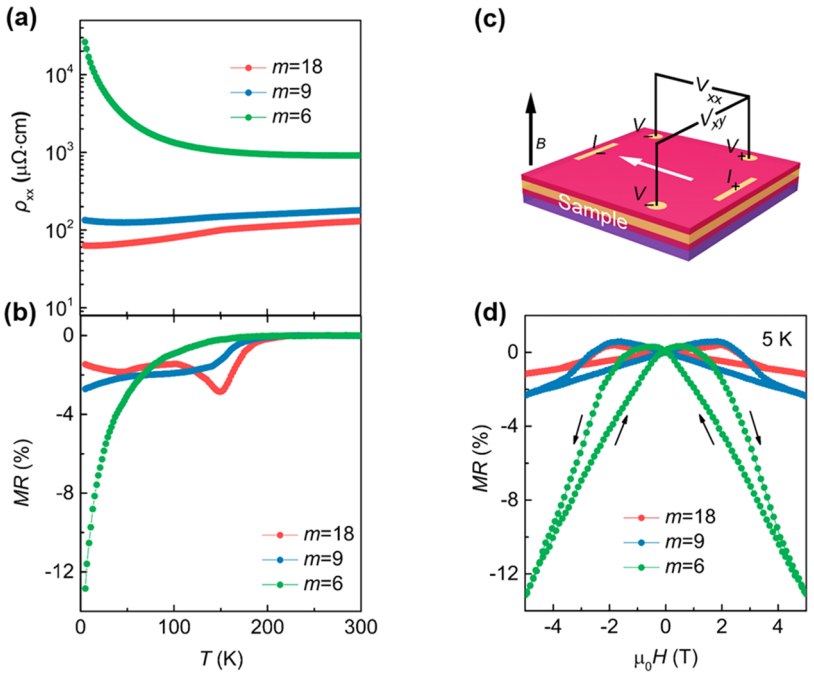

Figure 2. Transport properties of SRO/BFO multilayers. (a) Temperature-dependent ρ_{xx} of all multilayers measured at the zero field. (b) Temperature-dependent MR with a magnetic field applied normal to the plane of the multilayers. (c) Schematic of the experimental setup for transport measurements. (d) Magnetic field dependence of MR measured at 5 K. Arrows denote the field-sweeping direction.

mission electron microscopy (STEM), and the THE arising from the broken inversion symmetry of the SRO structure was observed. We further discussed the origin of the THE and the magnetic contributions from the interfacial and middle SRO regions.

2. RESULTS AND DISCUSSION

Figure 1a–c shows the configurations of the designed multilayers with a stacking order of $BFO_{12}/(SRO_m/BFO_{12})_n$ grown on $SrTiO_3$ (STO) (001) substrates, where the thickness (m u.c.) of the SRO layer varies systematically, while the BFO layer is fixed at 12 u.c. In our multilayers, the thickness of the SRO layer is chosen as m = 18, 9, and 6 u.c., whereas the total thickness of SRO is kept at 18 u.c. by designing the corresponding periodic repetitions of building blocks. The surface topography of the STO substrate (Figure S1) shows an atomically flat TiO_2-terminated surface, which provides a basic condition for the growth of high-quality multilayer thin films. X-ray diffraction (XRD) θ–2θ scans of the multilayers were performed to examine the quality of the samples, as shown in Figures 1d and S2. The observed satellite peaks around the main reflection suggest high interface quality and the structural coherence of the multilayers. Furthermore, X-ray reciprocal space mappings (RSMs) around the STO (103) diffraction condition were measured, as shown in Figure 1e. All multilayers are fully strained on STO substrates and possess a coherent in-plane lattice parameter as that of STO substrates (3.905 Å). The average c-axis lattice constants of BFO and SRO (Figure S3) extracted from the corresponding $(002)_{pc}$ Bragg reflection are larger than those of bulk BFO (3.96 Å) and bulk SRO (3.93 Å),[30−35] where the subscript pc denotes the pseudocubic notation. This suggests that both SRO and BFO in the multilayers are elongated along the out-of-plane direction. In general, the mismatch strain can be released with increasing film thickness. However, our results show a larger out-of-plane lattice constant of SRO in the thicker multilayer (with smaller m), which can be related to the strong modulation of structural parameters of SRO near the BFO/SRO interface (details are discussed later).

Atomic structures of the multilayers were illustrated by high-angle annular dark-field STEM (HAADF-STEM) images. A representative HAADF-STEM image for the m = 9 multilayer is shown in Figure 1g. There is no apparent misfit dislocations at the interfaces. Strikingly, a displacement between the B-site Ru and the mass center of the four nearest A-site cations is observed in SRO near the BFO/SRO interfaces, as shown in the insets of Figure 1g. It is demonstrated that the ferroelectric-driven ionic displacements in BFO can penetrate into SRO, suggesting a ferroelectric proximity effect. The HAADF-STEM intensity profiles of the A- and B-site cations obtained from the selected atomic columns in Figure 1g are plotted in Figure 1h. We can see that the ionic displacements induced by the ferroelectric proximity effect can cross the heterointerface and penetrate into SRO to a depth of 2–3 u.c. Thus, the interfacial SRO regions with ionic displacements can be distinguished from the middle SRO layer, as schematically shown in Figure 1f. Figure 1i displays the evolution of the layer-by-layer polar displacements ($\delta_{Fe/Ru}$) along the [001] axis near the BFO/SRO interfaces of the m = 9 multilayer. Positive (negative) $\delta_{Fe/Ru}$ denotes the upward (downward) direction of the ionic displacement. The larger top and bottom δ_{Fe} induced sizable δ_{Ru} within a depth of 3 u.c. near the BFO/SRO interfaces. Moreover, the ionic displacements in the interfacial SRO regions have also been observed in the m = 18 and 6 multilayers (Figures S4 and S5). The ferroelectric proximity effect has been reported in ferroelectric/SRO heterointerfaces, as a result of the softness of the SRO lattice that provides an efficient mechanism of polarization screening.[36−38] In our multilayers, the ionic displacements in the interfacial SRO regions are modulated by the ferroelectric polarization of BFO,

https://doi.org/10.1021/acsami.1c21703
ACS Appl. Mater. Interfaces 2022, 14, 6194−6202

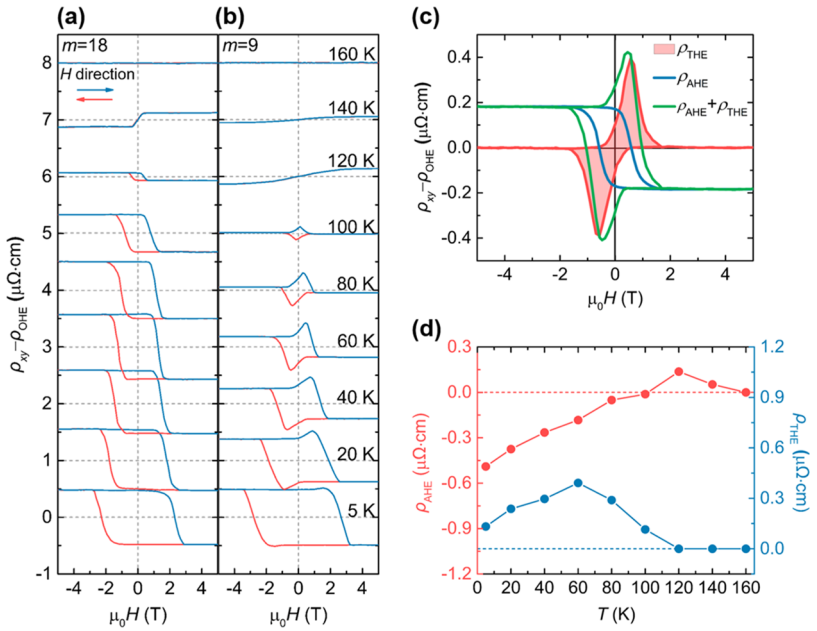

Figure 3. Observation of THE in the SRO/BFO multilayers. The Hall resistivity as a function of magnetic field for the (a) m = 18 and (b) m = 9 samples at various temperatures. The data in (a, b) are shifted vertically for clarity. Red and blue in (a, b) represent the field-sweeping direction. (c) ρ_{xy}, ρ_{AHE}, and ρ_{THE} versus H for the m = 9 sample at 60 K. (d) Temperature dependence of ρ_{AHE} and ρ_{THE} for the m = 9 sample.

and thus, the ferroelectricity of BFO has directly coupled to the metallic SRO layer. As a result, the observed ionic displacements supposedly have a large influence on the transport and magnetic properties of interfacial SRO regions.

The longitudinal resistivity (ρ_{xx}) and Hall resistivity (ρ_{xy}) of the multilayers were measured with a typical geometry, as shown in Figure 2c. Figure 2a shows the temperature dependence of ρ_{xx} for the three multilayers. For the m = 18 sample, we observe a metallic behavior down to the lowest temperature. A cusp in the ρ_{xx} (T) curve at ∼150 K indicates the phase transition to the ferromagnetic state. The curve for the m = 9 sample exhibits higher resistivity and a small upturn below 47 K, demonstrating the occurrence of a metal-to-insulator transition. In addition, a slightly weak cusp at ∼140 K is observed for the m = 9 sample, indicating that T_c reduces with the decrease of m. For the m = 6 sample, the resistivity at low temperatures increases more than 2 orders of magnitude and presents an obvious insulating state. The cusp corresponding to the ferromagnetic transition for the m = 6 sample becomes indistinguishable. Therefore, the emergence of the insulating state occurs at multilayers with SRO thicknesses of 6−9 u.c., which is larger than the reported thickness of 3−4 u.c. for the SRO single layer grown on STO substrates.[10,11] This result suggests that the structural disorder in the interfacial SRO induced by the ferroelectric proximity effect would give rise to the insulating behavior. Moreover, we cannot rule out the presence of non-zero net charges at the BFO/SRO interfaces that result in an intrinsic build-in field across the interfaces. Electronic reconstructions may happen within the interfacial SRO layers, which might also have an effect on transport behavior.

Figure 2b shows the temperature dependence of magnetoresistance [MR = $(\rho_H - \rho_0)/\rho_0$], which was measured at the magnetic fields of 0 and 5 T along the pseudocubic [001] direction. For the ferromagnetic state of SRO, the domain wall resistance has a dominant contribution to the MR, leading to the observed negative MR under the fields.[39] The MR valleys, which are known to correspond to T_c of SRO, shift to lower temperatures with decreasing m. This is consistent with the shift of the cusps in Figure 2a. The decrease of T_c can be ascribed to the enhanced structure disorder near the BFO/SRO interfaces.[40] Figure 2d shows the out-of-plane MR measured at 5 K for the multilayers with various m. For all of the samples, a standard negative MR with a butterfly-shaped hysteresis is observed. Additionally, the magnetic field dependence of MR of all of the multilayers measured at different temperatures is shown in Figure S6. The butterfly-shaped feature decays with increasing temperature, reflecting the suppressed ferromagnetic ordering in SRO. Furthermore, the feature of MR also shows that the SRO layers in the multilayers are subject to an in-plane compressive strain and have a magnetic easy axis along the out-of-plane direction.[41]

The magnetic field dependence of ρ_{xy} at different temperatures was further investigated to probe the interface effects on the transport response of the multilayers. In general, the Hall resistivity can be decomposed into $\rho_{xy} = \rho_{OHE} + \rho_{AHE} + \rho_{THE}$, where the first term represents the ordinary Hall resistivity ($\rho_{OHE} = R_0H$) proportion to the out-of-plane magnetic field (H) and the second term represents the anomalous Hall resistivity ($\rho_{AHE} = R_SM$) proportion to magnetization (M). Thereinto, R_0 and R_S are the ordinary and anomalous Hall coefficients, respectively. The third term is attributed to the THE contribution, arising from the real-space Berry phase that is acquired by conduction electrons, as they travel through a non-coplanar spin texture. Figure 3 shows the Hall measurements for the multilayers. The ordinary Hall effect (OHE) contribution has been subtracted by linear fitting of the magnetic field dependence of ρ_{xy} in the range of $\mu_0H \geq 3.0$ T. As shown in Figure 3a, the m = 18 sample in a temperature range from 5 to 120 K is similar to an inverted magnetic hysteresis loop, signifying a dominant AHE with negative R_S. As the temperature increases to 140 K, the sign of R_S changes to positive. Such an anomalous sign change is thought to be associated with the changes in the momentum space Berry

https://doi.org/10.1021/acsami.1c21703
ACS Appl. Mater. Interfaces 2022, 14, 6194−6202

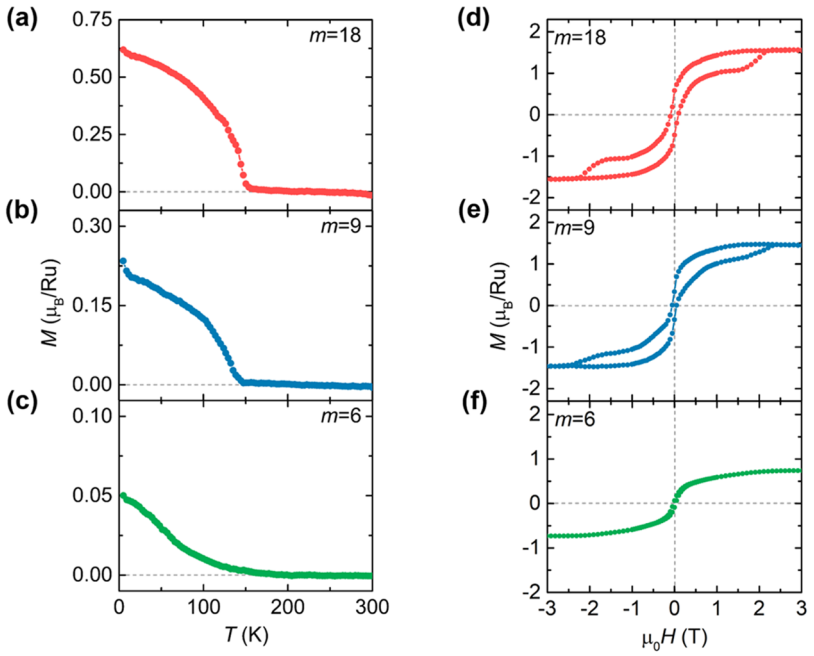

Figure 4. Magnetic evolutions in the SRO/BFO multilayers. The temperature dependence of magnetization measured at 5 K of (a) m = 18, (b) m = 9, and (c) m = 6 samples. The measurements were taken after field cooling in 0.02 T. The magnetic hysteresis loops of (d) m = 18, (e) m = 9, and (f) m = 6 samples. All magnetic measurements were taken with the magnetic fields applied in the out-of-plane direction of the STO substrate.

curvature near the Fermi level.[17,42,43] With increasing temperature, the AHE feature is gradually suppressed and finally vanishes near the ferromagnetic transition temperature, demonstrating the magnetic origin of AHE.

Figure 3b shows the Hall measurement for the m = 9 sample. Two abnormal humps are observed in the ρ_{xy} (H) curves below ∼100 K. Several studies have demonstrated the similar hump structures in SRO thin films when combined with a spin−orbit coupling layer $SrIrO_3$[15] or ferroelectric layer.[14,16,19,20] This hump feature has been assigned to the third term THE, where the DMI, which is the driving force for the formation of magnetic skyrmions, stems from the broken inversion symmetry by inequivalent interfaces in SRO thin films. In our case, ferroelectric-driven ionic displacements in the interfacial SRO layers break the inversion symmetry of the SRO structure, giving rise to an interfacial DMI. The degree of broken inversion symmetry in SRO can be determined by the ionic displacement between Ru and O in the RuO_2 plane. The Hamiltonian of the DMI can be defined as $H_{DMI} = \mathbf{D}_{12} \cdot (\mathbf{S}_1 \times \mathbf{S}_2)$,[16] where the DMI vector $\mathbf{D}_{12}$ is perpendicular to the Ru−O−Ru chains. Here, $\mathbf{S}_1$ and $\mathbf{S}_2$ are two neighboring spins in SRO. For a ferroelectrically distorted SRO layer, the calculated $|\mathbf{D}_{12}|$ value increases with the ionic displacement between Ru and O chains.[18] The δ_{Ru} values near the top and bottom BFO/SRO interfaces, as shown in Figure 1i, are up to ∼0.12 Å along the out-of-plane direction. The polar displacement is larger than that of the BTO/SRO bilayer system with robust skyrmions stabilized by a strong DMI.[16] In addition, previous work reported that the THE in the SRO/BFO bilayer system can be manipulated by the modulation of interlayer exchange coupling and interfacial DMI induced by ferroelectric polarization. Based on the above scenario, we conclude that the hump structures in the ρ_{xy} (H) curves for the m = 9 multilayer can be reasonably assigned to the THE with a skyrmion nature, although the possibility that the additional humps are related to two-channel AHE signals cannot be ruled out directly. The THE signal can be obtained by fitting and subtracting the AHE signal because ρ_{AHE} is proportion to magnetization. Figure 3c shows a typically separated AHE and THE contributions for the m = 9 multilayer measured at 60 K. When the sweeping field from ±5 T approaches the coercive field (H_C), the THE increases sharply and reaches the maximum values at approximately ±0.5 T. When the sweeping field further traverses H_C, the THE gradually decreases to zero at a field of around ±1.8 T, where the inverted M (H) loop (AHE with negative R_S) closes also. This strongly suggests that the THE occurs when the ferromagnetic domains begin switching. The summarized ρ_{AHE} and ρ_{THE} as a function of temperature are shown in Figure 3d. We note that the sign reversal of AHE also appears in the m = 9 sample with increasing temperature. The amplitude of the THE increases with increasing temperature in the range from 5 K to below ∼60 K and then decreases to zero at ∼120 K. No THE is observed in the m = 18 sample because the effective interfacial DMI reduces with the increase of m and the spins of SRO cannot be twisted to realize magnetic skyrmions.[15] For the m = 6 sample, Hall signals were not detected because of its insulating characteristics.

To further investigate the Hall origin, we measured the magnetism of the three samples. It is known that the Fe^{3+} ions in BFO are antiferromagnetic ordering and their moments describe a cycloid with a period of 62 nm.[44] Here, the weak ferromagnetism of BFO layers due to spin canting by the tilting of the oxygen octahedral[45] is neglected. Figure 4a−c shows the temperature dependence of field-cooled magnetization for the m = 18, 9, and 6 samples. The m = 18 sample shows a normal paramagnetic-to-ferromagnetic phase transition. When m decreases to 9, the phase transition shifts to a lower temperature and the magnetization reduces clearly. When m further decreases to 6, the sample shows quenched magnetization with no clear Curie transition. The phase transition behaviors are in agreement with that revealed by the temperature dependences of ρ_{xx} and MR shown in Figure

https://doi.org/10.1021/acsami.1c21703
ACS Appl. Mater. Interfaces 2022, 14, 6194−6202

2a,b, indicating that the ferromagnetic state is relatively destabilized with decreasing m. Figure 4d–f shows the M (H) loops for the m = 18, 9, and 6 samples at 5 K. The m = 18 and 9 samples in Figure 4d,e show an unusual step-like behavior, whereas the loop for the m = 6 sample, as shown in Figure 4f, presents a slim shape with a small H_C value and weak saturation magnetization. Loops with step-like features are similar to the hysteresis loop of the bilayer system with soft (small H_C) and hard (large H_C) magnetic phases.[46] In our multilayers, we can divide the M (H) loops of the m = 18 and 9 samples into two components with small and large H_C, respectively. By comparison with the ρ_{xy} (H) curves at 5 K shown in Figure 3a,b, it can be deduced that the component with large H_C can be attributed to the middle SRO regions rather than the interfacial SRO regions because interfacial regions exhibit the insulating state that almost has no contribution to ρ_{xy}. When m decreases to 6, the M (H) loops only have soft magnetic phases contributed from interfacial SRO regions. This is consistent with the HAADF-STEM result that the SRO layer with a thickness of 2–3 u.c. near the BFO/SRO interfaces is modified by the ferroelectric proximity effect.

The magnetic properties of ultrathin SRO films are strongly dependent on their structural symmetry, which can be determined by the RuO_6 octahedral tilting. Meng et al.[21] revealed a similar step-like behavior in the M (H) loops of BTO/SRO heterostructures and considered that this behavior originated from the discrepancy of structural distortions in the interfacial and middle SRO regions, which is induced by the ferroelectric proximity effect. The previous study suggests that tetragonal SRO shows uniaxial perpendicular anisotropy with large out-of-plane H_C, whereas monoclinic SRO exhibits longitudinal anisotropy with small out-of-plane H_C due to the canted magnetization.[47] The monoclinic phase can be transformed to the tetragonal phase by controlling the RuO_6 octahedral distortion in SRO.[48,49] Additionally, Jeong et al. suggested that the tetragonal phase of the SRO layer in SRO/BTO superlattices exhibits higher T_c and larger H_C compared to the orthorhombic phase.[50] In our multilayers, ultrathin SRO layers fully strained on STO substrates should have exhibited the tetragonal phase. However, an additional geometric constraint induced by the ferroelectric proximity effect would be imposed to trigger the structural distortion of SRO layers near the interfaces. This ferroelectric-driven lattice distortion of SRO causes the RuO_6 octahedral tilting while elongating the lattice along the out-of-plane direction. As m decreases to 6, the entire ultrathin SRO layers are controlled by the ferroelectric proximity effect, thus resulting in larger c-axis lattice parameters. Thus, the SRO near the interfaces can be an orthorhombic phase with slight monoclinic distortion and shows a small H_C value. In addition, oxygen vacancies inevitably exist in oxide multilayers. Lu et al. recently reported that in the SRO thin films grown on STO substrates with high-concentration oxygen vacancies, the oxygen-deficient SRO near the interface is a ferromagnetic insulator with small H_C, while the above SRO is a ferromagnetic metal with large H_C.[18] Thus, in our multilayers, the possible accumulation of oxygen vacancies in the interfacial SRO regions may also contribute to the observed magnetic behavior.

3. CONCLUSIONS

In summary, we report the unusual transport and magnetic properties in SRO/BFO multilayers. The ferroelectric proximity effect has been confirmed by the observation of Ru ionic displacements in interfacial SRO regions. Furthermore, THE with a skyrmion nature is observed in the m = 9 multilayer, arising from the broken inversion symmetry of the SRO structure near the BFO/SRO interface. The magnetic results further suggest that the interfacial SRO regions exhibit smaller H_C compared to that of the middle SRO region, which can be attributed to an additional geometric constraint induced by the ferroelectric proximity effect. Our work opens the door to further explore functional oxide heterointerfaces that potentially exhibit novel physical properties at the atomic scale.

4. EXPERIMENTAL SECTION

4.1. Sample Preparation. Epitaxial SRO/BFO multilayers were grown on TiO_2-terminated STO (001) substrates by laser molecular beam epitaxy (Pascal system). A focused pulsed excimer laser with a wavelength of 308 nm was employed to irradiate the ceramic BFO and SRO targets alternatively at a fixed energy density of ~1.5 J/cm^2 and a repetition of 2 Hz. All multilayers were grown at a substrate temperature of around 640 °C under an oxygen pressure of 10 Pa. After the deposition, all samples were in situ annealed for 10 mins and then cooled down to room temperature at a rate of 10 °C/min.

4.2. Structural Characterization. The surface topography of the atomically flat TiO_2-terminated STO substrates was characterized by atomic force microscopy (AFM, Asylum Research MFP-3D) equipped with Ti/Ir-coated silicon tips. High-resolution XRD θ–2θ scans and reciprocal space mappings (RSMs) of the samples were performed using an X-ray diffractometer (Rigaku SmartLab) equipped with a 9 kW rotating anode X-ray source ($\lambda \sim 1.54$ Å). HAADF images of all of the multilayers were acquired by an aberration-corrected STEM (JEOL ARW-300F) working at an accelerating voltage of 300 kV.

4.3. Measurements of Transport and Magnetic Properties. Transport measurements were performed using a physical property measurement system (PPMS, Quantum Design) in a conventional four-terminal configuration, as shown in Figure 2c. The magnetization data were recorded by a magnetic property measurement system (MPMS, Quantum Design) with a magnetic field applied perpendicularly to the surface plane.

■ ASSOCIATED CONTENT

Supporting Information

The Supporting Information is available free of charge at https://pubs.acs.org/doi/10.1021/acsami.1c21703.

AFM images of the TiO_2-terminated STO (001) substrate; XRD θ–2θ scans of SRO/BFO multilayers; c-axis lattice parameters of BFO and SRO as a function of m; atomic-scale high-resolution HAADF-STEM image and the corresponding intensity and polar displacement profiles for the m = 18 sample; atomic-scale high-resolution HAADF-STEM image and the corresponding intensity and polar displacement profiles for the m = 6 sample; and magnetic field dependence of MR at different temperatures of SRO/BFO multilayers (PDF)

■ AUTHOR INFORMATION

Corresponding Authors

Can Wang – *Beijing National Laboratory for Condensed Matter Physics, Institute of Physics, Chinese Academy of Sciences, Beijing 100190, China; School of Physical Sciences, University of Chinese Academy of Sciences, Beijing 100049, China; Songshan Lake Materials Laboratory, Dongguan, Guangdong 523808, China;* orcid.org/0000-0002-4404-7957; Email: canwang@iphy.ac.cn

https://doi.org/10.1021/acsami.1c21703
ACS Appl. Mater. Interfaces 2022, 14, 6194–6202

Kui-juan Jin − *Beijing National Laboratory for Condensed Matter Physics, Institute of Physics, Chinese Academy of Sciences, Beijing 100190, China; School of Physical Sciences, University of Chinese Academy of Sciences, Beijing 100049, China; Songshan Lake Materials Laboratory, Dongguan, Guangdong 523808, China;* orcid.org/0000-0002-0047-4375; Email: kjjin@iphy.ac.cn

Authors

Xiaokang Yao − *Beijing National Laboratory for Condensed Matter Physics, Institute of Physics, Chinese Academy of Sciences, Beijing 100190, China; School of Physical Sciences, University of Chinese Academy of Sciences, Beijing 100049, China*

Er-Jia Guo − *Beijing National Laboratory for Condensed Matter Physics, Institute of Physics, Chinese Academy of Sciences, Beijing 100190, China; School of Physical Sciences, University of Chinese Academy of Sciences, Beijing 100049, China; Songshan Lake Materials Laboratory, Dongguan, Guangdong 523808, China;* orcid.org/0000-0001-5702-225X

Xinyan Wang − *Beijing National Laboratory for Condensed Matter Physics, Institute of Physics, Chinese Academy of Sciences, Beijing 100190, China; School of Physical Sciences, University of Chinese Academy of Sciences, Beijing 100049, China*

Xiaomei Li − *Beijing National Laboratory for Condensed Matter Physics, Institute of Physics, Chinese Academy of Sciences, Beijing 100190, China; School of Physical Sciences, University of Chinese Academy of Sciences, Beijing 100049, China; International Center for Quantum Materials, School of Physics, Peking University, Beijing 100871, China*

Lei Liao − *Beijing National Laboratory for Condensed Matter Physics, Institute of Physics, Chinese Academy of Sciences, Beijing 100190, China; School of Physical Sciences, University of Chinese Academy of Sciences, Beijing 100049, China*

Yong Zhou − *Beijing National Laboratory for Condensed Matter Physics, Institute of Physics, Chinese Academy of Sciences, Beijing 100190, China; School of Physical Sciences, University of Chinese Academy of Sciences, Beijing 100049, China*

Shan Lin − *Beijing National Laboratory for Condensed Matter Physics, Institute of Physics, Chinese Academy of Sciences, Beijing 100190, China; Center of Materials Science and Optoelectronics Engineering, University of Chinese Academy of Sciences, Beijing 100049, China*

Qiao Jin − *Beijing National Laboratory for Condensed Matter Physics, Institute of Physics, Chinese Academy of Sciences, Beijing 100190, China; School of Physical Sciences, University of Chinese Academy of Sciences, Beijing 100049, China*

Chen Ge − *Beijing National Laboratory for Condensed Matter Physics, Institute of Physics, Chinese Academy of Sciences, Beijing 100190, China; School of Physical Sciences, University of Chinese Academy of Sciences, Beijing 100049, China;* orcid.org/0000-0002-8093-940X

Meng He − *Beijing National Laboratory for Condensed Matter Physics, Institute of Physics, Chinese Academy of Sciences, Beijing 100190, China*

Xuedong Bai − *Beijing National Laboratory for Condensed Matter Physics, Institute of Physics, Chinese Academy of Sciences, Beijing 100190, China; School of Physical Sciences, University of Chinese Academy of Sciences, Beijing 100049, China; Songshan Lake Materials Laboratory, Dongguan, Guangdong 523808, China;* orcid.org/0000-0002-1403-491X

Peng Gao − *International Center for Quantum Materials, School of Physics, Peking University, Beijing 100871, China;* orcid.org/0000-0003-0860-5525

Guozhen Yang − *Beijing National Laboratory for Condensed Matter Physics, Institute of Physics, Chinese Academy of Sciences, Beijing 100190, China; School of Physical Sciences, University of Chinese Academy of Sciences, Beijing 100049, China*

Complete contact information is available at: https://pubs.acs.org/10.1021/acsami.1c21703

Author Contributions

X.Y. conceived and designed the research, grew the samples, performed structural characterization, carried out the transport measurement, measured magnetic properties, analyzed the data, and wrote the manuscript. C.W. conceived and designed the research, analyzed the data, wrote the manuscript, and guided the project. E.G. provided valuable suggestions for the manuscript. X.W. analyzed the data. X.L. and L.L. performed STEM experiments. Y.Z. participated in the discussion of transport measurement. S.L. and Q.J. participated in the discussion of magnetic measurement. C.G. and M.H. participated in the discussion of sample synthesis. X.B. and P.G. supervised the STEM measurement. G.Y. participated in the discussion of the manuscript. K.J.: guided the project. All authors have given approval to the final version of the manuscript.

Notes

The authors declare no competing financial interest.

■ ACKNOWLEDGMENTS

This work was supported by the National Key Basic Research Program of China (Grant Nos. 2017YFA0303604, 2019YFA0308500, 2020YFA0309100, and 2021YFA1400700), the National Natural Science Foundation of China (Grant Nos. 12174437, 11874412, 11721404, 12074416, 11974390, 51672307, 51991344, 52025025, and 52072400), the Beijing Nova Program of Science and Technology (Grant No. Z191100001119112), the Beijing Natural Science Foundation (Grant Nos. Z190010 and 2202060), the Youth Innovation Promotion Association of Chinese Academy of Sciences (Grant No. 2018008), and the Strategic Priority Research Program of Chinese Academy of Sciences (Grant No. XDB33030200).

■ REFERENCES

(1) Ohtomo, A.; Hwang, H. A High-Mobility Electron Gas at the $LaAlO_3/SrTiO_3$ Heterointerface. *Nature* **2004**, *427*, 423−426.

(2) Gozar, A.; Logvenov, G.; Kourkoutis, L. F.; Bollinger, A. T.; Giannuzzi, L. A.; Muller, D. A.; Bozovic, I. High-Temperature Interface Superconductivity between Metallic and Insulating Copper Oxides. *Nature* **2008**, *455*, 782−785.

(3) Reyren, N.; Thiel, S.; Caviglia, A. D.; Kourkoutis, L. F.; Hammerl, G.; Richter, C.; Schneider, C. W.; Kopp, T.; Rüetschi, A.-S.; Jaccard, D.; Gabay, M.; Muller, D. A.; Triscone, J.-M.; Mannhart, J. Superconducting Interfaces between Insulating Oxides. *Science* **2007**, *317*, 1196−1199.

(4) Cai, K.; Yang, M.; Ju, H.; Wang, S.; Ji, Y.; Li, B.; Edmonds, K. W.; Sheng, Y.; Zhang, B.; Zhang, N.; Liu, S.; Zheng, H.; Wang, K.

Electric Field Control of Deterministic Current-Induced Magnetization Switching In a Hybrid Ferromagnetic/Ferroelectric Structure. *Nat. Mater.* **2017**, *16*, 712−716.
(5) Kanbayasi, A. Magnetic Properties of $SrRuO_3$ Single Crystal. *J. Phys. Soc. Jpn.* **1976**, *41*, 1876−1878.
(6) Jones, C. W.; Battle, P. D.; Lightfoot, P.; Harrison, W. T. A. The Structure of $SrRuO_3$ by Time-of-Flight Neutron Powder Diffraction. *Acta Crystallogr., Sect. C: Cryst. Struct. Commun.* **1989**, *45*, 365−367.
(7) Vailionis, A.; Siemons, W.; Koster, G. Room Temperature Epitaxial Stabilization of a Tetragonal Phase in *A*RuO3 (*A*=Ca and Sr) Thin Films. *Appl. Phys. Lett.* **2008**, *93*, No. 051909.
(8) Koster, G.; Klein, L.; Siemons, W.; Rijnders, G.; Dodge, J. S.; Eom, C. B.; Blank, D. H. A.; Beasley, M. R. Structure, Physical Properties, and Applications of SrRuO3 Thin Films. *Rev. Mod. Phys.* **2012**, *84*, 253−298.
(9) Toyota, D.; Ohkubo, I.; Kumigashira, H.; Oshima, M.; Ohnishi, T.; Lippmaa, M.; Takizawa, M.; Fujimori, A.; Ono, K.; Kawasaki, M.; Koinuma, H. Thickness-Dependent Electronic Structure of Ultrathin Films Studied by *in Situ* Photoemission Spectroscopy. *Appl. Phys. Lett.* **2005**, *87*, No. 162508.
(10) Shen, X.; Qiu, X.; Su, D.; Zhou, S.; Li, A.; Wu, D. Thickness-Dependent Metal-Insulator Transition in Epitaxial $SrRuO_3$ Ultrathin Films. *J. Appl. Phys.* **2015**, *117*, No. 015307.
(11) Xia, J.; Siemons, W.; Koster, G.; Beasley, M. R.; Kapitulnik, A. Critical Thickness for Itinerant Ferromagnetism in Ultrathin Films of $SrRuO_3$. *Phys. Rev. B* **2009**, *79*, No. 140407.
(12) Fert, A.; Reyren, N.; Cros, V. Magnetic Skyrmions: Advances in Physics and Potential Applications. *Nat. Rev. Mater.* **2017**, *2*, No. 17031.
(13) Li, Z.; Shen, S.; Tian, Z.; Hwangbo, K.; Wang, M.; Wang, Y.; Bartram, F. M.; He, L.; Lyu, Y.; Dong, Y.; Wan, G.; Li, H.; Lu, N.; Zang, J.; Zhou, H.; Arenholz, E.; He, Q.; Yang, L.; Luo, W.; Yu, Pu. Reversible Manipulation of the Magnetic State in $SrRuO_3$ through Electric-Field Controlled Proton Evolution. *Nat. Commun.* **2020**, *11*, No. 184.
(14) Seddon, S. D.; Dogaru, D. E.; Holt, S. J. R.; Rusu, D.; Peters, J. J. P.; Sanchez, A. M.; Alexe, M. Real-Space Observation of Ferroelectrically Induced Magnetic Spin Crystal in $SrRuO_3$. *Nat. Commun.* **2021**, *12*, No. 2007.
(15) Matsuno, J.; Ogawa, N.; Yasuda, K.; Kagawa, F.; Koshibae, W.; Nagaosa, N.; Tokura, Y.; Kawasaki, M. Interface-Driven Topological Hall Effect in $SrRuO_3$-$SrIrO_3$ Bilayer. *Sci. Adv.* **2016**, *2*, No. e1600304.
(16) Wang, L.; Feng, Q.; Kim, Y.; Kim, R.; Lee, K. H.; Pollard, S. D.; Shin, Y. J.; Zhou, H.; Peng, W.; Lee, D.; Meng, W.; Yang, H.; Han, J.; Kim, M.; Lu, Q.; Noh, T. W. Ferroelectrically Tunable Magnetic Skyrmions in Ultrathin Oxide Heterostructures. *Nat. Mater.* **2018**, *17*, 1087−1094.
(17) Qin, Q.; Liu, L.; Lin, W.; Shu, X.; Xie, Q.; Lim, Z.; Li, C.; He, S.; Chow, G. M.; Chen, J. S. Emergence of Topological Hall Effect in a $SrRuO_3$ Single Layer. *Adv. Mater.* **2019**, *31*, No. 1807008.
(18) Lu, J.; Si, L.; Zhang, Q.; Tian, C.; Liu, X.; Song, C.; Dong, S.; Wang, J.; Cheng, S.; Qu, L.; Zhang, K.; Shi, Y.; Huang, H.; Zhu, T.; Mi, W.; Zhong, Z.; Gu, L.; Held, K.; Wang, L.; Zhang, J. Defect-Engineered Dzyaloshinskii−Moriya Interaction and Electric-Field-Switchable Topological Spin Texture in $SrRuO_3$. *Adv. Mater.* **2021**, *33*, No. 2102525.
(19) Wang, H.; Dai, Y.; Liu, Z.; Xie, Q.; Liu, C.; Lin, W.; Liu, L.; Yang, P.; Wang, J.; Venkatesan, T. V.; Chow, G. M.; Tian, H.; Zhang, Z.; Chen, J. Overcoming the Limits of the Interfacial Dzyaloshinskii−Moriya Interaction by Antiferromagnetic Order in Multiferroic Heterostructures. *Adv. Mater.* **2020**, *32*, No. 1904415.
(20) Gu, Y.; Song, C.; Zhang, Q.; Li, F.; Tan, H.; Xu, K.; Li, J.; Saleem, M. S.; Fayaz, M. U.; Peng, J.; Hu, F.; Gu, L.; Liu, W.; Zhang, Z.; Pan, F. Interfacial Control of Ferromagnetism in Ultrathin $SrRuO_3$ Films Sandwiched between Ferroelectric $BaTiO_3$ Layers. *ACS Appl. Mater. Interfaces* **2020**, *12*, 6707−6715.
(21) Meng, M.; Wang, Z.; Fathima, A.; Ghosh, S.; Saghayezhian, M.; Taylor, J.; Jin, R.; Zhu, Y.; Pantelides, S. T.; Zhang, J.; Plummer, E. W.; Guo, H. Interface-Induced Magnetic Polar Metal Phase in Complex Oxides. *Nat. Commun.* **2019**, *10*, No. 5248.
(22) van Thiel, T. C.; Brzezicki, W.; Autieri, C.; Hortensius, J. R.; Afanasiev, D.; Gauquelin, N.; Jannis, D.; Janssen, N.; Groenendijk, D. J.; Fatermans, J.; Van Aert, S.; Verbeeck, J.; Cuoco, M.; Caviglia, A. D. Coupling Charge and Topological Reconstructions at Polar Oxide Interfaces. *Phys. Rev. Lett.* **2021**, *127*, No. 127202.
(23) Wang, L.; Feng, Q.; Lee, H. G.; Ko, E. K.; Lu, Q.; Noh, T. W. Controllable Thickness Inhomogeneity and Berry Curvature Engineering of Anomalous Hall Effect in $SrRuO_3$ Ultrathin Films. *Nano Lett.* **2020**, *20*, 2468−2477.
(24) Kimbell, G.; Sass, P. M.; Woltjes, B.; Ko, E. K.; Noh, T. W.; Wu, W.; Robinson, J. W. A. Two-channel anomalous Hall effect in $SrRuO_3$. *Phys. Rev. Mater.* **2020**, *4*, No. 054414.
(25) Ren, Z. Y.; Shao, F.; Liu, P. F.; Wang, M. X.; Chen, J. K.; Meng, K. K.; Xu, X. G.; Miao, J.; Jiang, Y. Nonvolatile Ferroelectric Field Control of the Anomalous Hall Effect in $BiFeO_3$/$SrRuO_3$ Bilayer. *Phys. Rev. Appl.* **2020**, *13*, No. 024044.
(26) Ko, E. K.; Lee, H. G.; Lee, S.; Mun, J.; Kim, J.; Lee, J. H.; Kim, T. H.; Chung, J. S.; Chung, S. B.; Park, S. H.; Yang, S. M.; Kim, M.; Chang, S. H.; Noh, T. W. Tunable Two-Channel Magnetotransport in $SrRuO_3$ Ultrathin Films Achieved by Controlling the Kinetics of Heterostructure Deposition. *Adv. Electron. Mater.* **2021**, *7*, No. 2100804.
(27) Wang, J.; Neaton, J. B.; Zheng, H.; Nagarajan, V.; Ogale, S. B.; Liu, B.; Viehland, D.; Vaithyanathan, V.; Schlom, D. G.; Waghmare, U. V.; Spaldin, N. A.; Rabe, K. M.; Wuttig, M.; Ramesh, R. Epitaxial $BiFeO_3$ Multiferroic Thin Film Heterostructures. *Science* **2003**, *299*, 1719−1722.
(28) Spaldin, N. A.; Ramesh, R. Advances in Magnetoelectric Multiferroics. *Nat. Mater.* **2019**, *18*, 203−212.
(29) Spaldin, N. A.; Cheong, S. W.; Ramesh, R. Multiferroics: Past, Present, and Future. *Phys. Today* **2010**, *63*, 38−43.
(30) Gan, Q.; Rao, R. A.; Eom, C. B.; Garrett, J. L.; Lee, M. Direct Measurement of Strain Effects on Magnetic and Electrical Properties of Epitaxial $SrRuO_3$ Thin Films. *Appl. Phys. Lett.* **1998**, *72*, 978−980.
(31) Infante, I. C.; Lisenkov, S.; Dupé, B.; Bibes, M.; Fusil, S.; Jacquet, E.; Geneste, G.; Petit, S.; Courtial, A.; Juraszek, J.; Bellaiche, L.; Barthélémy, A.; Dkhil, B. Bridging Multiferroic Phase Transitions by Epitaxial Strain in $BiFeO_3$. *Phys. Rev. Lett.* **2010**, *105*, No. 057601.
(32) Choi, T.; Lee, S.; Choi, Y. J.; Kiryukhin, V.; Cheong, S. W. Switchable Ferroelectric Diode and Photovoltaic Effect in $BiFeO_3$. *Science* **2009**, *324*, 63−66.
(33) Lee, S.; Ratcliff, W., II; Cheong, S. W.; Kiryukhin, V. Electric Field Control of the Magnetic State in $BiFeO_3$ Single Crystals. *Appl. Phys. Lett.* **2008**, *92*, No. 192906.
(34) Lee, S.; Choi, T.; Ratcliff, W., II; Erwin, R.; Cheong, S. W.; Kiryukhin, V. Single Ferroelectric and Chiral Magnetic Domain of Single-Crystalline $BiFeO_3$ in an Electric Field. *Phys. Rev. B* **2008**, *78*, No. 100101.
(35) Jang, H. W.; Baek, S. H.; Ortiz, D.; Folkman, C. M.; Das, R. R.; Chu, Y. H.; Shafer, P.; Zhang, J. X.; Choudhury, S.; Vaithyanathan, V.; Chen, Y. B.; Felker, D. A.; Biegalski, M. D.; Rzchowski, M. S.; Pan, X. Q.; Schlom, D. G.; Chen, L. Q.; Ramesh, R.; Eom, C. B. Strain-Induced Polarization Rotation in Epitaxial (001) $BiFeO_3$ Thin Films. *Phys. Rev. Lett.* **2008**, *101*, No. 107602.
(36) Gerra, G.; Tagantsev, A. K.; Setter, N.; Parlinski, K. Ionic Polarizability of Conductive Metal Oxides and Critical Thickness for Ferroelectricity in $BaTiO_3$. *Phys. Rev. Lett.* **2006**, *96*, No. 107603.
(37) Chisholm, M. F.; Luo, W. D.; Oxley, M. P.; Pantelides, S. T.; Lee, H. N. Atomic-Scale Compensation Phenomena at Polar Interfaces. *Phys. Rev. Lett.* **2010**, *105*, No. 197602.
(38) Ye, M.; Hu, S.; Zhu, Y.; Zhang, Y.; Ke, S.; Xie, L.; Zhang, Y.; Hu, S.; Zhang, D.; Luo, Z.; Gu, M.; He, J.; Zhang, P.; Zhang, W.; Chen, L. Electric Polarization Switching on an Atomically Thin Metallic Oxide. *Nano Lett.* **2021**, *21*, 144−150.
(39) Klein, L.; Kats, Y.; Marshall, A. F.; Reiner, J. W.; Geballe, T. H.; Beasley, M. R.; Kapitulnik, A. Domain Wall Resistivity in $SrRuO_3$. *Phys. Rev. Lett.* **2000**, *84*, 6090−6093.

https://doi.org/10.1021/acsami.1c21703
ACS Appl. Mater. Interfaces 2022, 14, 6194−6202

(40) Herranz, G.; Martinez, B.; Fontcuberta, J.; Sanchez, F.; Ferrater, C.; Garcia-Cuenca, M. V.; Varela, M. Enhanced Electron-Electron Correlations in Nanometric $SrRuO_3$ Epitaxial Films. *Phys. Rev. B* **2003**, *67*, No. 174423.
(41) Tian, D.; Liu, Z.; Shen, S.; Li, Z.; Zhou, Y.; Liu, H.; Chen, H.; Yu, P. Manipulating Berry Curvature of $SrRuO_3$ Thin Films via Epitaxial Strain. *Proc. Natl. Acad. Sci. U.S.A.* **2021**, *118*, No. e2101946118.
(42) Fang, Z.; Nagaosa, N.; Takahashi, K. S.; Asamitsu, A.; Mathieu, R.; Ogasawara, T.; Yamada, H.; Kawasaki, M.; Tokura, Y.; Terakura, K. The Anomalous Hall Effect and Magnetic Monopoles in Momentum Space. *Science* **2003**, *302*, 92−95.
(43) Wang, W.; Li, L.; Liu, J.; Chen, B.; Ji, Y.; Wang, J.; Cheng, G.; Lu, Y.; Rijnders, G.; Koster, G.; Wu, W.; Liao, Z. Magnetic Domain Engineering in $SrRuO_3$ Thin Films. *npj Quantum Mater* **2020**, *5*, No. 73.
(44) Lebeugle, D.; Colson, D.; Forget, A.; Viret, M.; Bataille, A. M.; Gukasov, A. Electric-Field-Induced Spin Flop in $BiFeO_3$ Single Crystals at Room Temperature. *Phys. Rev. Lett.* **2008**, *100*, No. 227602.
(45) Albrecht, D.; Lisenkov, S.; Ren, W.; Rahmedov, D.; Kornev, I. A.; Bellaiche, L. Ferromagnetism in Multiferroic $BiFeO_3$ Films: A First-Principles-Based Study. *Phys. Rev. B* **2010**, *81*, No. 140401.
(46) Fullerton, E. E.; Jiang, J. S.; Bader, S. D. Hard/soft magnetic heterostructures: model exchange-spring magnets. *J. Magn. Magn. Mater.* **1999**, *200*, 392−404.
(47) Qin, Q.; Song, W.; He, S.; Yang, P.; Chen, J. Magnetization Reversal and Magnetoresistance Behavior of Exchange Coupled $SrRuO_3$ Bilayer. *J. Phys. D: Appl. Phys.* **2017**, *50*, No. 215002.
(48) Lu, W.; Yang, P.; Song, W. D.; Chow, G. M.; Chen, J. S. Control of Oxygen Octahedral Rotations and Physical Properties in $SrRuO_3$ Films. *Phys. Rev. B* **2013**, *88*, No. 214115.
(49) Lu, W.; Song, W.; Yang, P.; Ding, J.; Chow, G. M.; Chen, J. S. Strain Engineering of Octahedral Rotations and Physical Properties of $SrRuO_3$ Films. *Sci. Rep.* **2015**, *5*, No. 10245.
(50) Jeong, S. G.; Han, G.; Song, S.; Min, T.; Mohamed, A. Y.; Park, S.; Lee, J.; Jeong, H. Y.; Kim, Y. M.; Cho, D. Y.; Choi, W. S. Propagation Control of Octahedral Tilt in $SrRuO_3$ via Artificial Heterostructuring. *Adv. Sci.* **2020**, *7*, No. 2001643.

https://doi.org/10.1021/acsami.1c21703
ACS Appl. Mater. Interfaces 2022, 14, 6194−6202